



# Impact of thick PMMA plates by long projectiles at low velocities. Part II: Effect of confinement

A. Dorogoy, D. Rittel\*

Faculty of Mechanical Engineering, Technion – Israel Institute of Technology, 32000 Haifa, Israel



## ARTICLE INFO

### Article history:

Received 30 June 2013

Received in revised form 16 October 2013

Available online 12 December 2013

### Keywords:

PMMA

Confinement

Finite elements

Impact

Long projectiles

Penetration

## ABSTRACT

A hybrid experimental–numerical investigation of the penetration process in unconfined and confined thick polymethylmethacrylate (PMMA) plates was carried out. The confinement was applied by insertion of the polymeric plate into a conical steel ring. The response of such plates to the impact of long hard steel projectiles having an ogive-head shape in the range of velocities of  $165 < V_0 < 260$  (m/s), was investigated experimentally. The results show that unconfined targets were perforated and broken due to combined effect of penetration and cracking. By contrast, the confined targets were not perforated and could withstand repeated impacts due to suppression of the brittle damage mechanism by the confinement. The tests were modeled using 3D explicit finite element analyses. A good agreement regarding the trajectory of the projectile and the depths of penetration was obtained. The numerical results show that the confinement introduces a negative triaxiality and even some plasticity within the confined plates prior to impact. The increase of plastic failure strain of the PMMA at negative triaxiality reduces the ductile damage during penetration, while the hydrostatic pressure reduces significantly the brittle fracture mechanism. The resisting force to the penetration depends on the failure strain–triaxiality relationship, and does not necessarily increase with higher confinement levels.

© 2013 Elsevier Ltd. All rights reserved.

## 1. Introduction

The creation of a self-equilibrated state of stress within an object or a structure is known as prestressing. This ancient technique is mainly aimed at strengthening a structure by applying confining forces. Presentation and explanations of structural issues that arise in the design and construction of prestressed systems can be found in Gasparini (2006), where common techniques and processes for prestressing are discussed and illustrated. Examples of external prestressing for the purpose of structural strengthening with steel and fiber reinforced polymers, as well as plate bonding, can be found in Nordin (2005). Materials such as concrete and ceramic have a very low tensile strength in comparison with their compressive

strength. Consequently the working range of such materials can be greatly increased by imposing a compressive confinement. Ceramic materials have long been considered for armor applications because of their high strength and low density. In Anderson and Royal-Timmons (1997), 99.5%-pure aluminum oxide tiles, 2.54-cm thick, were radially confined and impacted by long-rod projectiles at velocities of the order of 1.5 km/s. It was concluded that the ballistic performance of a ceramic tile improves with confinement. The maximum depth-of-penetration (DOP) into the backup steel cylinder was the measure of penetration performance. It was shown that the performance is velocity dependent, a tendency that decreases at high confinement levels. The experimental data for radially confined tiles agree quite well with other investigations. Modeling of thin and thick ceramic target configurations for two prestress levels (small and large), and two prestress states (radial and hydrostatic) was reported in Holmquist and Johnson (2005). In all cases, prestressing

\* Corresponding author. Tel.: +972 4 829 3261.

E-mail addresses: [rittel@technion.ac.il](mailto:rittel@technion.ac.il), [merittel@technion.ac.il](mailto:merittel@technion.ac.il) (D. Rittel).

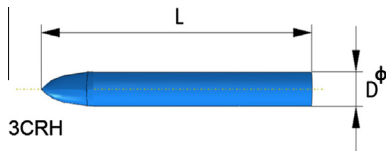


Fig. 1. The steel projectile having an ogive head corresponding to 3CRH.

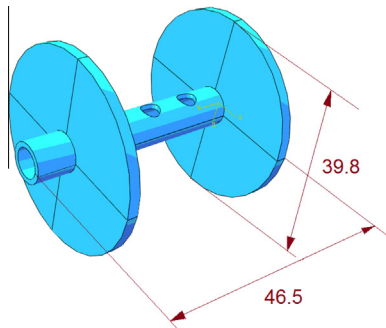


Fig. 2. A 3D scheme of the polymeric sabot.

the ceramic enhanced its ballistic performance, although the effect of the different prestress conditions on the ballistic response was not always obvious. In Holmquist and Johnson (2003), modeling showed that for complete penetration cases, the confinement decreases the exit velocity, and for partial penetration it decreases the depth of penetration. The development of transparent armor, which has many civilian and military applications, prompted the

investigation of the effect of confinement on transparent strong/hard glassy polymeric materials. However, experimental studies of that subject are still quite scarce. The failure mechanism of a PMMA layer subjected to a compressive pre-stress was recently investigated by Archer and Lesser (2009). This work addresses the effects of biaxial pre-stress. The shrink fit insertion technique was used to apply equi-biaxial confinement which maintains transparency of the target. A 102 mm diameter PMMA disk was inserted into a 12 mm thick ring made of carbon steel pipe. The radial mismatch between the inner radius of the steel ring and the PMMA disk ranged from 0.26 to 0.42 mm. The authors performed some preliminary ballistic impacts at speeds of  $\sim 130$  m/s and reported a significant reduction of radial cracking due to the pre-stress. While experimental results were reported, this study did not present a numerical model of the impact and penetration processes.

The present study extends and complements in a sense the work done in Archer and Lesser (2009) regarding the issue of ballistic impacts in confined PMMA, this material being selected because of its hardness and strength in the group of transparent glassy polymers. It consists of a hybrid *experimental-numerical* investigation of the effect of *high pre-stress* (radial mismatch of 1–1.5 mm in comparison to 0.26 to 0.42 mm in Archer and Lesser (2009)) on the ballistic performance of thick PMMA monolithic plates subjected to ballistic impacts of long ogive head projectiles traveling in *higher velocities* in the range of 165–260 (m/s). A conical insertion technique is used to apply and reach high levels of pre-stress.

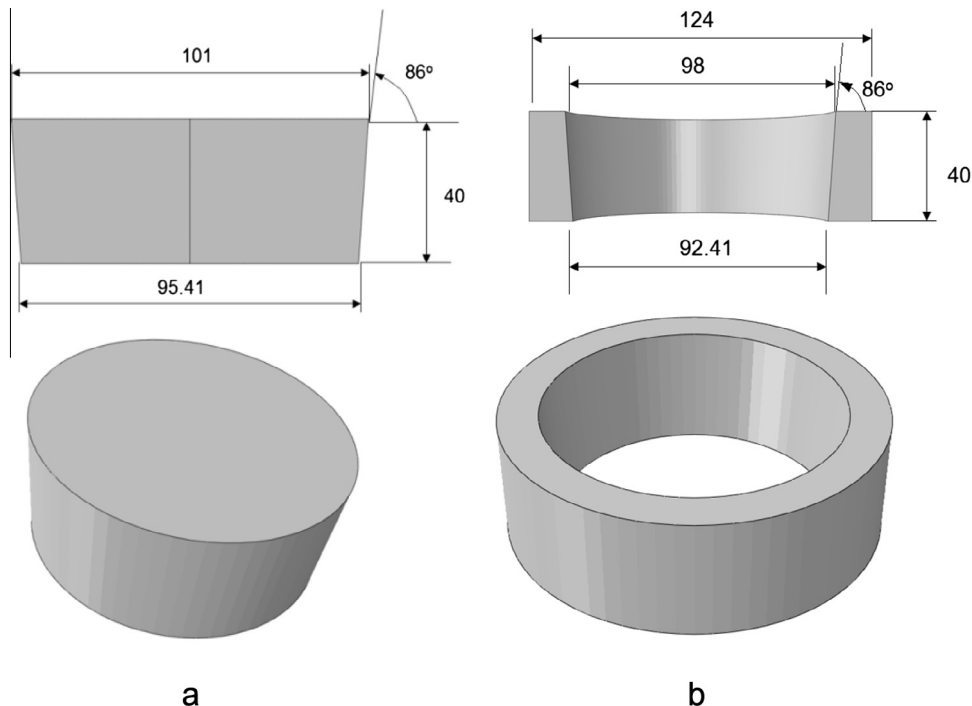


Fig. 3. (a) The round PMMA plate. (b) The confining steel ring.

The paper is organized in the following way: First the experimental setup is detailed, followed by the experimental results. The experimental results of the unconfined targets are shown first followed by the experimental results of confined targets. Next the numerical model is described shortly, followed by the simulations' results. A discussion comes next, followed by conclusions.

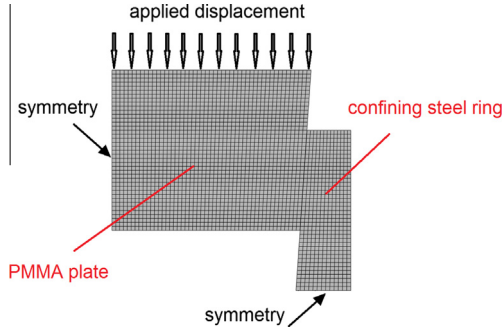


Fig. 4. The meshed axisymmetric model.

## 2. Experimental setup

Thick PMMA plates were impacted by long hard steel projectiles. The projectiles were accelerated by a gas gun. The procedure is fully detailed in part I of this work (Rittel and Dorogoy, 2013). The projectiles are stabilized in their flight by means of a polymeric sabot which gets destroyed upon impact. Two types of target plates were impacted: confined and unconfined. The projectile, sabot and targets are detailed in the sequel.

### 2.1. Projectile

The projectile which is shown in Fig. 1 was made of hard steel and weighted 11.4 (gr). It had a diameter  $D = 6$  (mm) and length  $L = 56$  (mm). Its head was ogive-shaped corresponding to 3CRH (Caliber Radius Head). Its dimensions correspond to the non-dimensional values  $L/D = 9.3$  which are considered as “long” projectiles (typical AP projectiles has  $3 < L/D < 5$ ). The same projectile was used in part I of this work (Rittel and Dorogoy, 2013), where it

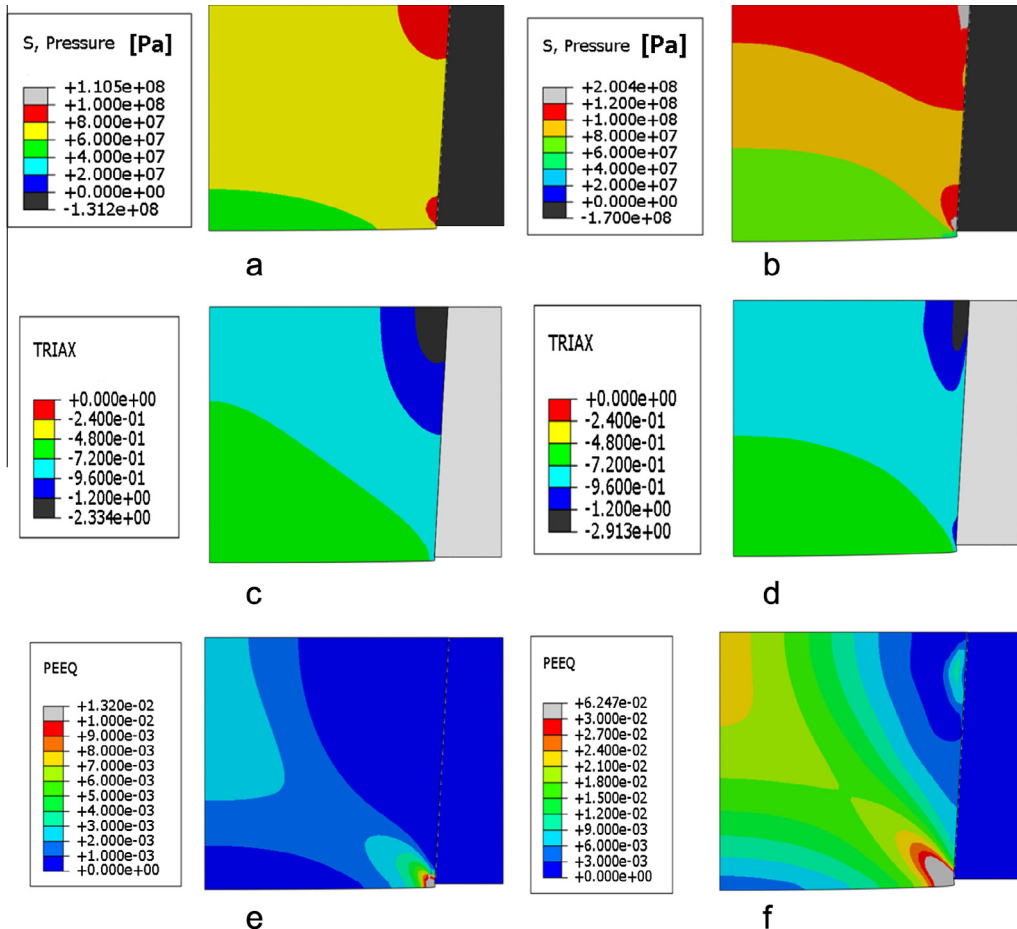


Fig. 5. Distributions of pressures (S), triaxialities (TRIAx) and equivalent plastic strains (PEEQ) within the two types of targets at the end of the insertion process. (a) Pressure distribution within 1st type target (lower confinement). (b) Pressure distribution within 2nd type target (higher confinement). (c) Triaxiality distribution within the 1st type target, (d) Triaxiality distribution within the 2nd type target. (e) Equivalent plastic strain distribution within the 1st type target. (f) Equivalent plastic strain distribution within the 2nd type target.

was noted that, out of three head geometries, the ogive one has the most deleterious effects on unconfined plates.

## 2.2. Sabot

The sabot is made by Objet 3D printer from FullCure720 which is a rigid, general purpose semi translucent acrylic-based photopolymer. It is similar in shape and dimensions to the one used in part I. The sabot is shown in Fig. 2 with its overall dimensions. Its weight is 6.5 (gr).

## 2.3. Confined targets

The confined plates were round with conic  $86^\circ$  side faces, as shown in Fig. 3(a). The plates were inserted into a confining steel sleeve (Fig. 3(b)) with an inner conic face of  $86^\circ$ . Two types of round PMMA plates were used. The types differed only by the size of the misfit between their outer radius and the inner radius of the confining ring, namely 1 (mm) (first type) and 1.5 (mm) (second type), respectively. The dimensions of the confining ring are shown in Fig. 3. The thickness of both the plates and the confining ring was 40 (mm). The plates are considered “thick” since  $t/D = 6.67$  where  $D$  is the projectile diameter (“thin” plates would correspond to  $t/D < 1$ ). The plates were inserted into the confining ring using an MTS servo-hydraulic machine. The maximum load needed for insertion of the 1st kind was  $\sim 23$  tons, while for the 2nd it reached 45 tons. The faces in contact were lubricated prior to insertion using silicone oil and water-displacing spray (WD40).

An axisymmetric numerical analysis was performed using Abaqus Standard version 12-2 (2012) to determine the resulting pressures, triaxialities and plastic strain within the two types of inserted plates. The axisymmetric model which consists of the PMMA plate and confining steel ring is shown in Fig. 4. Vertical displacements were applied on the upper face of the plate. Symmetry conditions were applied on the bottom face of the confining ring. Symmetry was also applied at  $r = 0$  (axisymmetric analysis). The meshed axisymmetric model of the 1st type target, shown in Fig. 4, consists of 1960 linear quadrilateral elements of type CAX4R on the PMMA plate. 520 linear quadrilateral elements of type CAX4R were used for the ring. The typical element size was  $\sim 1$  (mm). The variations of the pressure, triaxiality and plastic strains within the confined plates of both types upon completion of the insertion step are all detailed in Fig. 5. The pressure of the 1st and 2nd type targets are shown in Fig. 5(a) and (b) respectively. The pressure at the center of the 1st type target lies in the range 80–100 (MPa). The pressure at the center of the 2nd type target is slightly higher, and lies in the range 80–120 (MPa). The variation of triaxiality is detailed in Fig. 5(c) and (d) respectively. The triaxiality is defined as the ratio:  $t_r = \frac{\sigma_m}{\sigma_{eq}}$  where  $\sigma_m = \frac{\sigma_{II}}{3}$  and  $\sigma_{eq}$  is the Mises equivalent stress. It can be observed that the triaxiality ( $t_r$ ) is quite similar for the two types of targets and lies in the range of  $-0.96 < t_r < -0.72$ . This regime of triaxiality is just spread over a wider region for the 2nd type of target. Due to the high level of confinement, some plastic deformation develops inside the target. The plastic equivalent strain

variations are shown in Fig. 5(e) and (f) for each type of target, respectively. The center of the 1st type plate experiences plastic strains of 0.3%, while the 2nd type experiences plastic strains of 2.4%. The plasticity is much wider spread within the 2nd type target.

## 2.4. Unconfined targets

Two types of unconfined specimens were used: rectangular and round. The rectangular unconfined PMMA plate

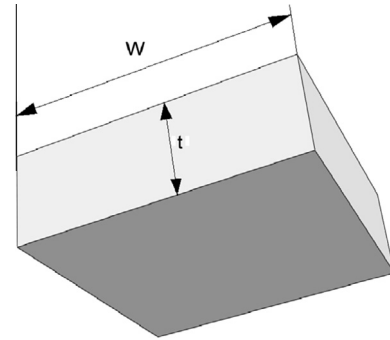


Fig. 6. The unconfined rectangular target.

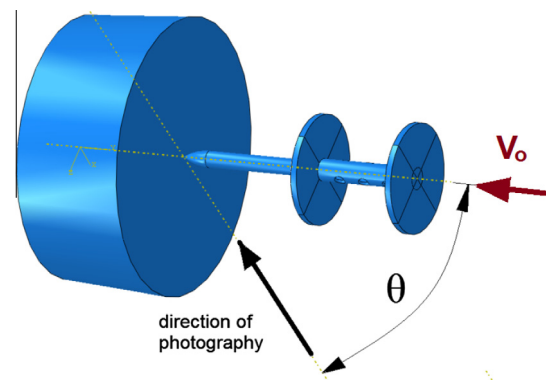
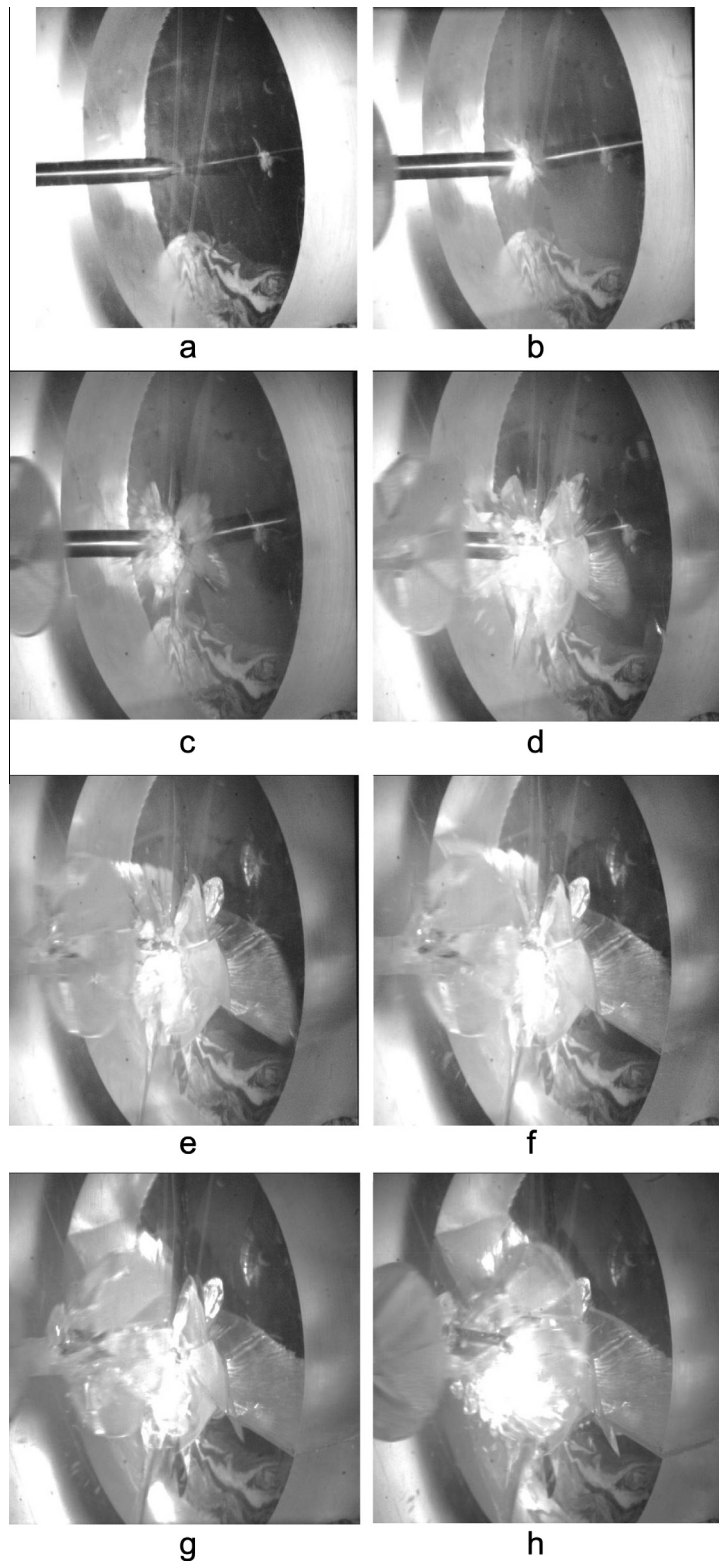


Fig. 7. Sketch of the assembly showing the sabot and the projectile just prior to impact. The direction of photography is inclined by an angle  $\theta$  to the line of fire.

Table 1

Experimental details of impact tests on unconfined targets.

Test	Target	Projectile	Impact velocity (m/s)	Remarks
1	Rectangular $w = 124$ (mm), $h = 40$ (mm)	Ogive	200	Perforated and broken
2	Rectangular $w = 124$ (mm), $h = 40$ (mm)	Ogive	230	Perforated and broken
3	Circular $D = 100$ (mm), $h = 33.6$ (mm)	Ogive	257	Perforated and broken
4	Circular $D = 100$ (mm), $h = 40$ (mm)	Ogive	243	Perforated and broken



**Fig. 8.** The penetration process of target 4 impacted at 243 (m/s). (a) Frame 00:  $t = 0.0$  ( $\mu\text{s}$ ). (b) Frame 02:  $t = 39.6$  ( $\mu\text{s}$ ). (c) Frame 04:  $t = 79.3$  ( $\mu\text{s}$ ). (d) Frame 06:  $t = 118.9$  ( $\mu\text{s}$ ). (e) Frame 08:  $t = 158.5$  ( $\mu\text{s}$ ). (f) Frame 09:  $t = 178.3$  ( $\mu\text{s}$ ). (g) Frame 10:  $t = 198.1$  ( $\mu\text{s}$ ). (h) Frame 13:  $t = 257.6$  ( $\mu\text{s}$ ). Note that fracture (shattering) is the reason for full perforation.



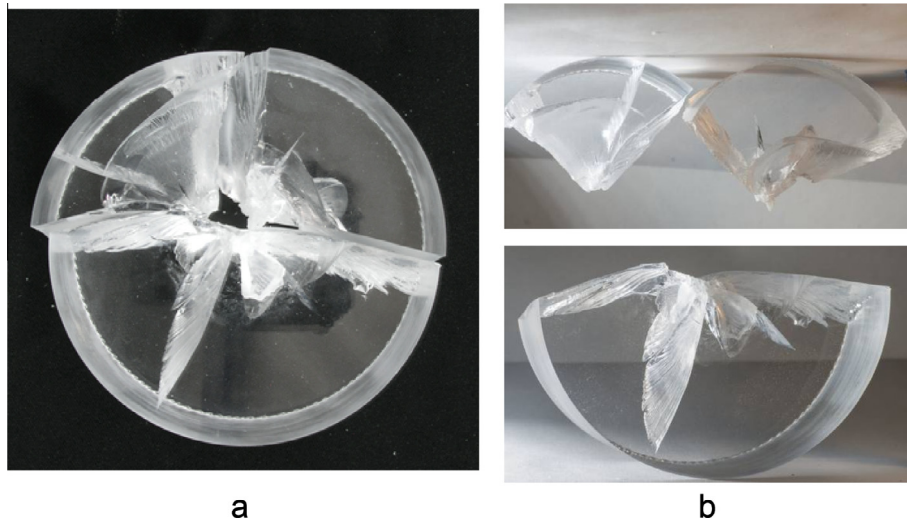


**Fig. 9.** The broken target 4. (a) The three main parts assembled. (b) The three main parts separately.

**Table 2**

Experimental details of impact tests on confined targets.

Test	Target	Projectile's head	Impact velocity (m/s)	Remarks
1	Circular 1st type $D = 101$ (mm), $h = 40$ (mm)	Ogive	230 Estimated	No perforation only penetration.
2	Circular 1st type $D = 101$ (mm), $h = 40$ (mm)	Ogive	202 Estimated	No perforation only penetration.
3	Circular 1st type $D = 101$ (mm), $h = 33.6$ (mm)	Ogive	232	No perforation only penetration.
4	Circular 2nd type $D = 102$ (mm), $h = 40$ (mm)	2 Ogive 2 hemispherical	167 Estimated	No perforation only penetration after 4 impacts.
5	Circular 2nd type $D = 102$ (mm), $h = 40$ (mm)	Ogive	243	No perforation only penetration.

had a width of  $W = 124$  (mm) and thickness  $t = 40$  (mm), as shown in Fig. 6. The same target was used in part I of this work. The round specimen was identical to the confined specimen shown in Fig. 3(a).

### 2.5. The assembly

The assembled projectile within its sabot just prior to impact is shown in Fig. 7. At that moment, the sabot and projectile have an initial impact velocity  $V_0$ . Helium gas pressurized to 12 (atm) was used to accelerate the projectile (and sabot) to  $V_0 \leq 260$  (m/s). The projectile was aimed at the center of the target. Since the confining steel ring of the confined targets is not transparent, the high speed camera (Cordin-530 – 200 kfps) was mounted at an inclined angle  $\theta$  to the line of fire as shown in Fig. 7. A total of 16 pictures were taken at time interval of  $\sim 20$  ( $\mu$ s) between each frame.

## 3. Experimental results

### 3.1. Experimental results of unconfined targets

Four impact tests were conducted on unconfined targets. Two targets were rectangular and the other two were

circular. Table 1 contains the experimental details. The velocities of tests 1 and 2 were estimated from the fast camera pictures. The velocities of tests 3 and 4 were measured by a velocity meter consisting of two photovoltaic cells which are mounted close to the outlet of the canon. All four targets were perforated and shattered into pieces due to the impact. The round targets were used in the tests for the sole purpose of comparing identical (round) plate geometries in two confinement states.

The penetration process of target 4, which is representative of all other tests, is detailed in Fig. 8(a)–(h). The fast camera took 16 frames (0–15) with an interval of 19.8 ( $\mu$ s) between each frame. Fig. 8(a) shows the projectile and target just before impact and this is referred as zero. A piece of plasticine that keeps the target upright is visible in the bottom of the back side of the target.

Fig. 8(b) shows that after 39.8 ( $\mu$ s) debris is flowing out of the crater while small cracks ahead of the projectile head are created. The manner in which the cracks are growing is detailed in Fig. 8(c)–(h). It can be observed in Fig. 8(f) that at time 178.3 ( $\mu$ s), the cracks have reached the circumferential face of the target and the target is already broken. The large cracks are mainly radial. When the sabot impact the target shown in Fig. 8(h) at time 257.6 ( $\mu$ s), it is already broken. Target #4 was broken into

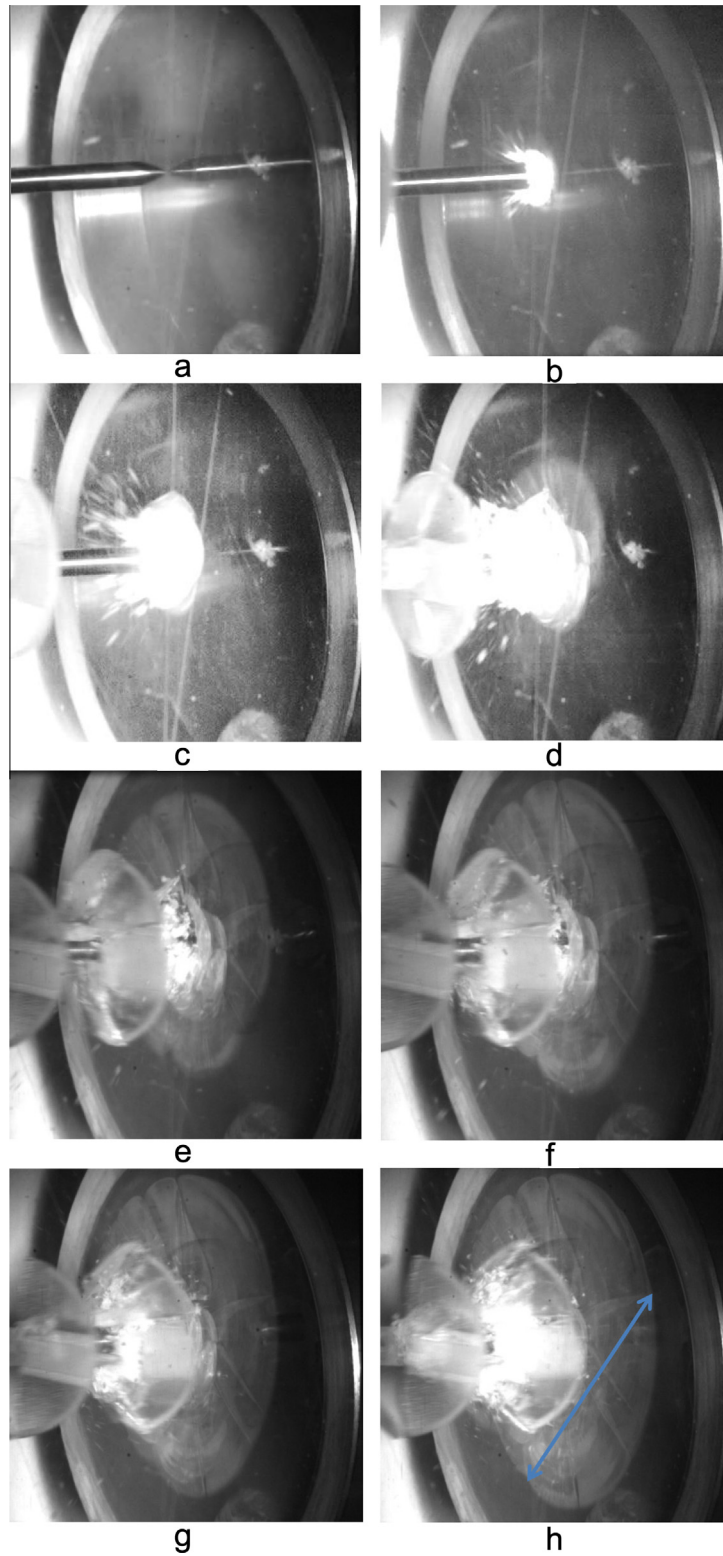


**Fig. 10.** Pictures of the process of penetration of an ogive projectile impacting at 243 (m/s) on target 5 of Table 2. (a)  $t = 0.0$  ( $\mu\text{s}$ ). (b)  $t = 39.6$  ( $\mu\text{s}$ ). (c)  $t = 79.3$  ( $\mu\text{s}$ ). (d)  $t = 138.7$  ( $\mu\text{s}$ ). (e)  $t = 198.1$  ( $\mu\text{s}$ ). (f)  $t = 217.9$  ( $\mu\text{s}$ ). (g)  $t = 237.8$  ( $\mu\text{s}$ ). (h)  $t = 257.6$  ( $\mu\text{s}$ ). Note the dish-like cracking (marked by arrow in Fig. 10(h)) and the shallow penetration. The propagation velocity of the dish-like cracks can be estimated from Fig 10(d)–(h).

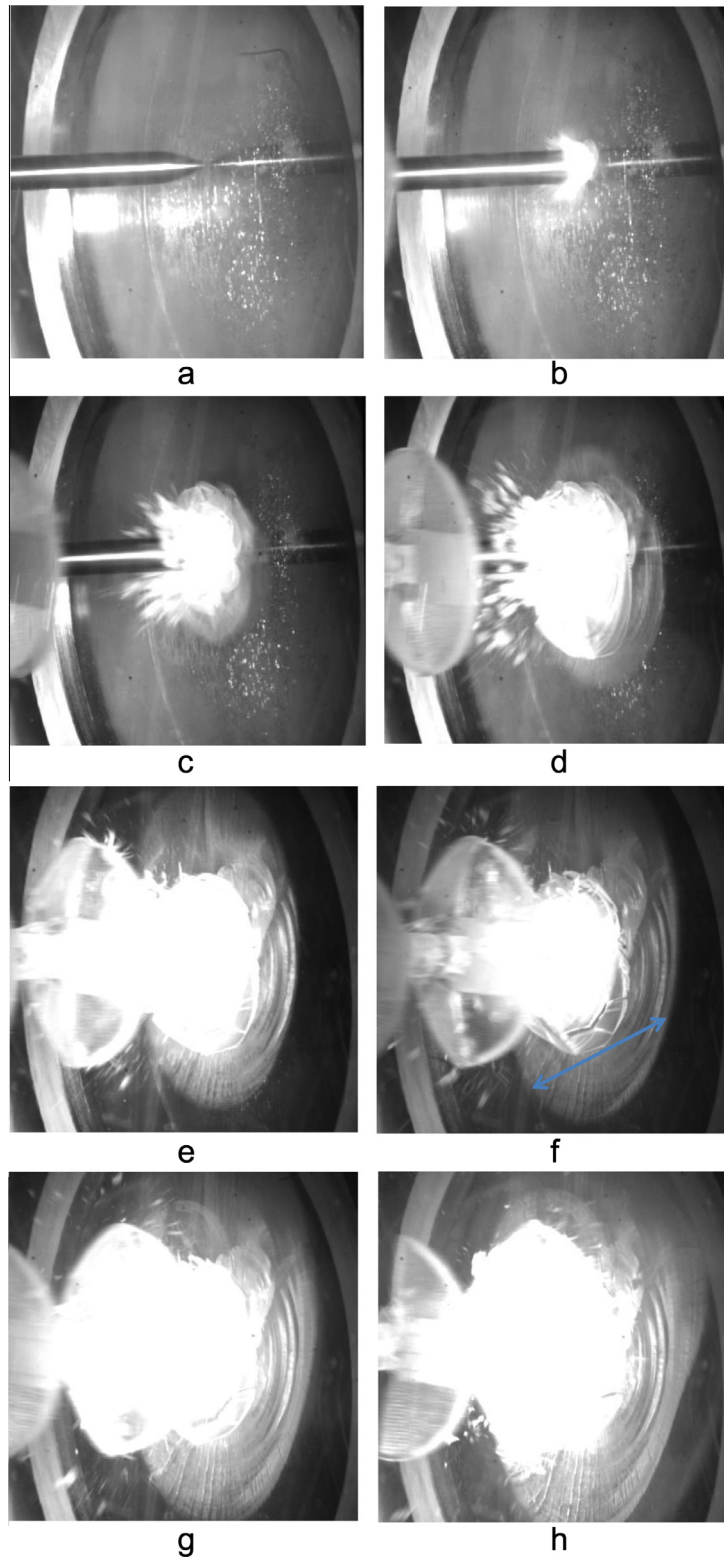


**Fig. 11.** Pictures of the process of penetration of an ogive projectile impacting at 232 (m/s) on target 3 of Table 2. (a)  $t = 0.0$  ( $\mu\text{s}$ ). (b)  $t = 39.4$  ( $\mu\text{s}$ ). (c)  $t = 78.5$  ( $\mu\text{s}$ ). (d)  $t = 118.1$  ( $\mu\text{s}$ ). (e)  $t = 157.5$  ( $\mu\text{s}$ ). (f)  $t = 177.2$  ( $\mu\text{s}$ ). (g)  $t = 196.9$  ( $\mu\text{s}$ ). (h)  $t = 236.3$  ( $\mu\text{s}$ ). Note the dish-like cracking (marked by arrow in Fig. 11(f)) and the shallow penetration.



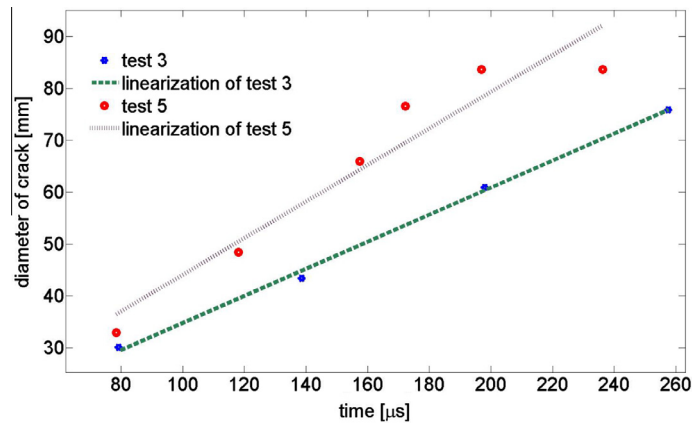


Fig. 12. The diameter of the main dish crack in targets 3 and 5 of Table 2 versus time.

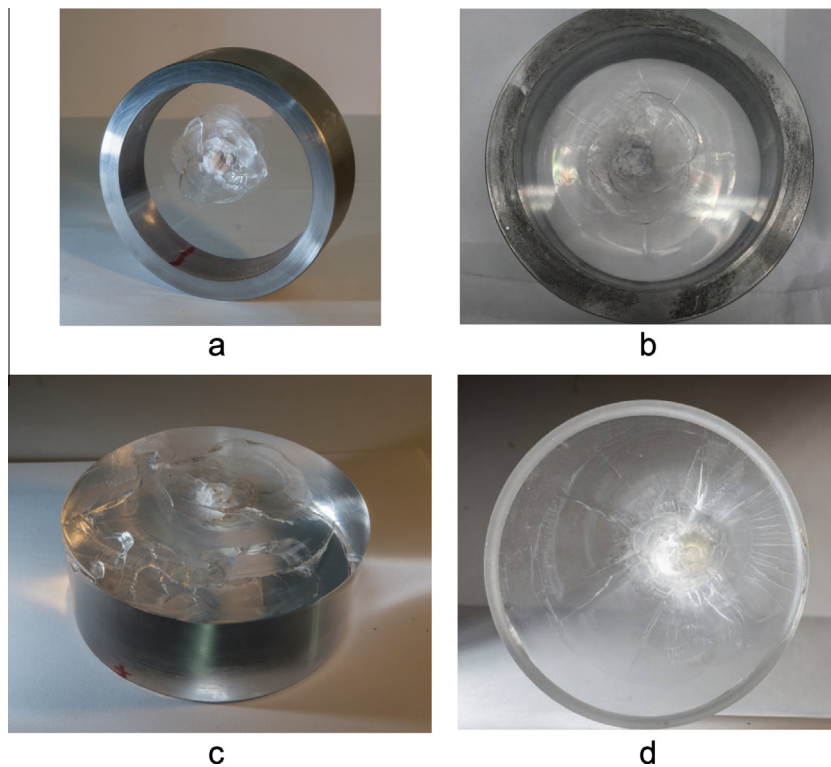


Fig. 13. Post failure front pictures of confined targets which are detailed in Table 2 showing the damage. (a) Target 1. (b) Target 4. (c) Target 2. (d) Target 5.

three main parts as shown in Fig. 9. A large brittle crack can be observed in the lower larger fragment of Fig. 9(b). From Figs. 8 and 9, it can be concluded that brittle fracture is actually the dominant mechanism that leads to the target's destruction, thus enabling full perforation.

### 3.2. Experimental results of confined targets

Five impact tests were conducted on confined targets. Three targets were of the 1st type (misfit of 1 (mm)) and two were of the 2nd type (misfit of 1.5 (mm)). Table 2 contains the experimental details. The impact velocities of

tests 1, 2 and 4 were estimated from the fast camera pictures. The velocities of tests 3 and 5 were measured by a velocity meter. None of the five targets was perforated or broken due the impact. Target number 4 even sustained 4 repeated impacts at  $V \sim 170$  (m/s), and was not fully perforated!

The penetration process into target 3 which is of the 1st type is detailed in Fig. 10(a)–(h). The penetration process into target 5 which is of the 2nd type is detailed in Fig. 11(a)–(h). The penetration processes shown in Figs. 10 and 11 are rather similar. After  $\sim 80$  ( $\mu$ s) cracks appear around the projectile's trajectory. These cracks look like

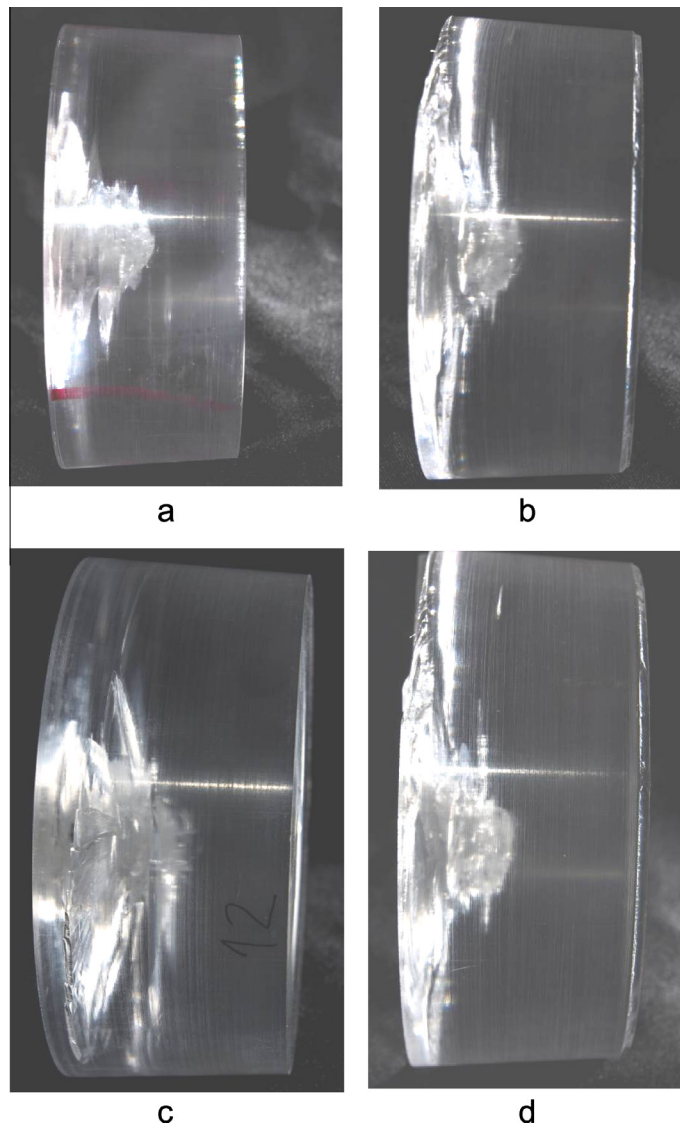


**Fig. 14.** Post failure side pictures of confined targets which are detailed in Table 2 showing the depth of penetration. (a) Target 1. (b) Target 2. (c) Target 3. (d) Target 5.

shallow dishes and propagate circumferentially toward the confined face and upwards toward the free impacted face. Fig. 12 shows the diameter of the main dish crack of targets 3 and 5 as a function of time. It appears that the diameter growth is quite steady with a velocity of  $\frac{\partial D}{\partial t} \approx 260 \frac{[m]}{[s]}$  in test 3 and  $\frac{\partial D}{\partial t} \approx 353 \frac{[m]}{[s]}$  for test 5. These values indicate that the crack front speed ( $D = 2r$ ) is half of the diameter expansion, and in the approximate range of  $130 \frac{[m]}{[s]} \leq \frac{\partial r}{\partial t} \leq 176 \frac{[m]}{[s]}$ . This velocity regime is in the range reported in Arakawa et al. (2000) and Loya et al. (2010).

Post-failure pictures of 4 of the confined targets are shown in Fig. 13. Targets 1 and 4 in Fig. 13(a) and (b) respectively are shown with the confining steel ring while targets 2 and 5 which are shown in Fig. 13(c) and (d) respectively are without the confining steel ring. The targets were not perforated or broken and could withstand

more impacts, Target 4 (not shown) was impacted 3 more times and was not fully perforated. Radial cracks which broke the unconfined plates are no longer evident. The cracking is in a dish-like manner and it does not penetrate deep into the target, but remains close to the free impacted face. It appears that the confinement suppresses brittle cracking and prevents it from penetrating deeper and shatter the targets. No significant difference between the 1st type and 2nd type targets are seen.

The depth of penetration is shown in Fig. 14 where the targets were stripped from their confining rings and side pictures perpendicular to the line of fire were taken. It can be observed that approximately half of the thickness of the PMMA plate ( $\sim 20$  mm) was penetrated. No significance difference between the two confinement levels are observed.

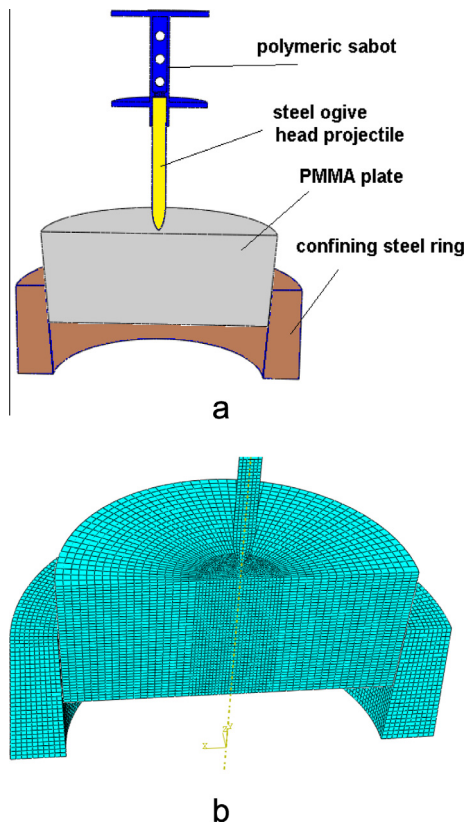


**Fig. 15.** (a) The assembled model at the beginning of the insertion step. (b) The meshed plate and ring.

#### 4. Numerical simulations

The numerical simulations of the round unconfined targets were performed in the same manner which is fully detailed in part I of this work (Rittel and Dorogoy, 2013) and will not be further reported here. The simulation of the confined targets was performed in two steps:

- (1) Insertion and confinement.
- (2) Impact.

Because of symmetry only half of the physical parts were modeled. Symmetry conditions were applied along the cut. Fig. 15(a) shows the assembly of the parts at the beginning of the insertion step. The insertion step is comparably long to avoid inertia effects and to mimic a quasi-static insertion. It lasts for 2000 ( $\mu$ s). It has been verified that the total kinetic energy within the target during the insertion step is negligible in comparison to the total internal energy. The (next) impact step lasts for 500 ( $\mu$ s). During the insertion step displacement are applied on the upper face of the PMMA plate while the bottom face of the confining ring is held fixed by application of symmetry conditions. Contact is assumed between all contacting surfaces. During most of the insertion step the sabot and projectile are held fixed. Close to the end of this step during the last 217 ( $\mu$ s), the sabot and projectile are accelerated

to 230 (m/s). At the end of the step the tip of the projectile almost touches the inserted PMMA plate. During the impact step, the displacement on the upper face of the plate, as well as the symmetry conditions on the bottom face of the ring, are released. Only the impact of the sabot and projectile having initial velocity, which was calculated in the previous step, act upon the confined target. The material models and failure parameters are the same as described in part I of this work (Rittel and Dorogoy, 2013). One difference regarding application of the elastic properties exists in this analysis with respect to the one done in Rittel and Dorogoy (2013). Here the elastic properties ( $E, \nu$ ) are applied with the aid of the user subroutine VUSDFLD and are strain-rate dependent. It was verified that during the insertion step, the quasi-static properties ( $E = 3.3$  (GPa),  $\nu = 0.35$ ) are used which yields the real confining pressures and triaxiality level. During the impact step, the strain rates are much higher and the dynamic values ( $E = 5.6$  (GPa),  $\nu = 0.42$ ) which were reported in Rittel and Maigre (1996) were applied for strain-rates of 100000 (1/s) and higher. For intermediate strain rates a linear interpolation between these values was used. The mesh characteristics are similar to those described in part I with a mesh size of 1 (mm) along the trajectory of the projectile as shown in Fig. 15(b).

#### 4.1. Numerical results

The numerical results in the sequel show the effect of the ductile failure strains and the extent of the misfit on the depth of penetration.

##### 4.1.1. Effect of equivalent failure strains

The impact of a 1st type plate was carried out using three different cases of ductile plastic failure strains. Fig. 16 shows the three types of the equivalent plastic failure strains. The failure strains in Fig. 16(a), designated as “Case I”, do not have a triaxiality dependency – they only depend on the strain rate which causes a small reduction of the value of the failure strain due to strain rate elevation. The failure strains shown in Fig. 16(b), named “Case II”, were used for calculations in this work. This case represents a linear increase of the failure strains with the negative triaxiality. Fig. 16(c) shows “Case III”, which is similar to “Case II”, but of a double extent.

The resultant depths of penetration for the three cases of failure strains, shown in Fig. 16, are plotted in Fig. 17. The depths of penetration of the tip of the projectiles' head are plotted. The failure strains of Case II seem to simulate well the ballistic tests, hence the displacements and time are normalized by the values at DOP value of the 1st type specimen ( $D = 100$  (mm), misfit of 1 (mm)) with Case II of plastic failure strains. The time is normalized by  $t_{type II}^{DOP} = 182$  ( $\mu$ s) and the depths of penetration by  $DOP_{type II} = 20.1$  (mm). By comparing the depth of penetration of the 1st type specimen due to the three cases of failure strains it can be concluded that the depths of penetration are strongly dependent on the failure strains. For failure strains of Case I the DOP is 24% deeper than for Case II. For Case III the DOP is 15% less than for Case II. The “bounce back effect” is evident in all three cases.

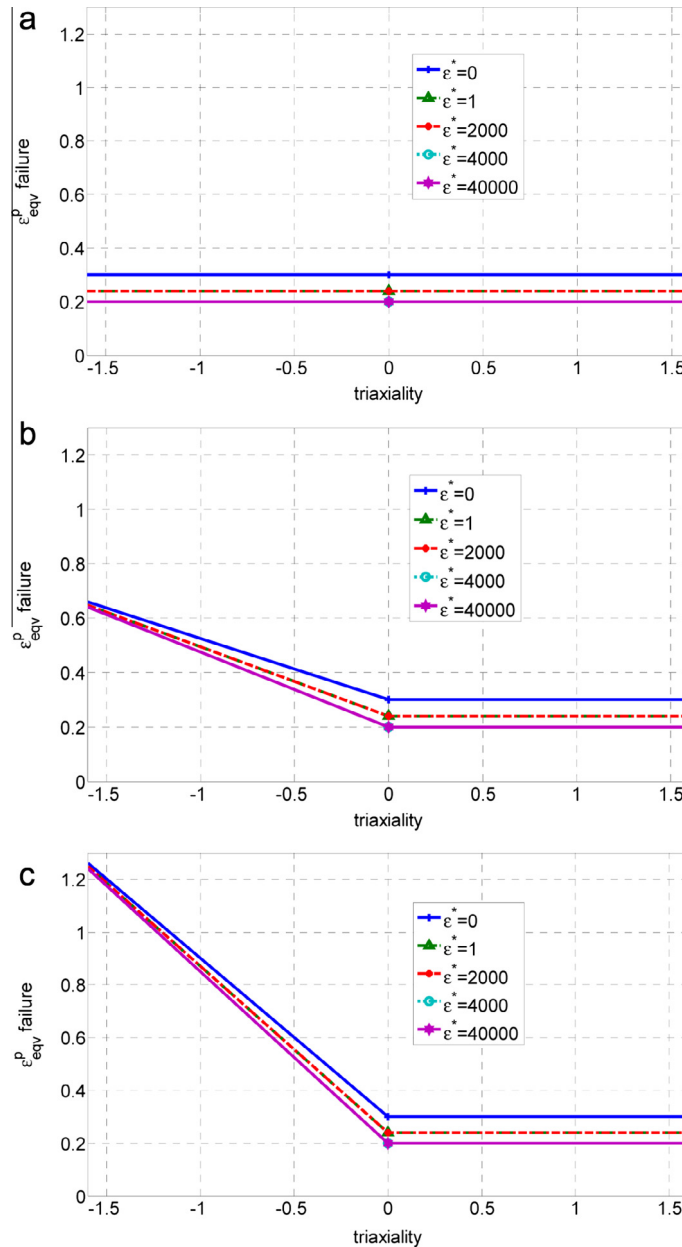


**Fig. 16.** Equivalent plastic failure strains vs triaxiality for various strain rates. (a) Case I – no dependence on triaxiality. (b) Case II – negative triaxiality cause linear elevation of the failure strains. (c) Case III – negative triaxiality cause linear elevation of the failure strains which are twice those of Case II.

#### 4.1.2. Effect of misfit

The impact into three types of targets which differ only by the amount of misfit with the confining ring diameter, have been simulated numerically. The ductile failure criteria used the Case II failure strain dependence on triaxiality (Fig. 16(b)). Two of the targets' types are the 1st and 2nd type which were tested experimentally. A 3rd type, which has a smaller misfit, is added to the numerical analyses. This type was not tested experimentally and is added to the numerical analyses only to further investigate the effect of the misfit. Their diameters were 100, 101 and 99 (mm) respectively, which correspond to a misfit of 1, 1.5

and 0.5 (mm). The resultant depths of penetration for the three types of targets are shown in Fig. 18. The targets details and their DOP are summarized in Table 3. The DOPs are normalized and compared with the value of the 1st type target which is the smallest.

The 2nd type target (1.5 (mm) misfit) sustains the highest pressure prior to impact. The 3rd type target (0.5 (mm) misfit) sustains the lowest pressure prior to impact. The minimum penetration is achieved for the 1st type target having an *intermediate* confinement. The DOP of the 2nd type target with the greatest confinement is 17% greater than DOP of the 1st target. The DOP of the 3rd type target

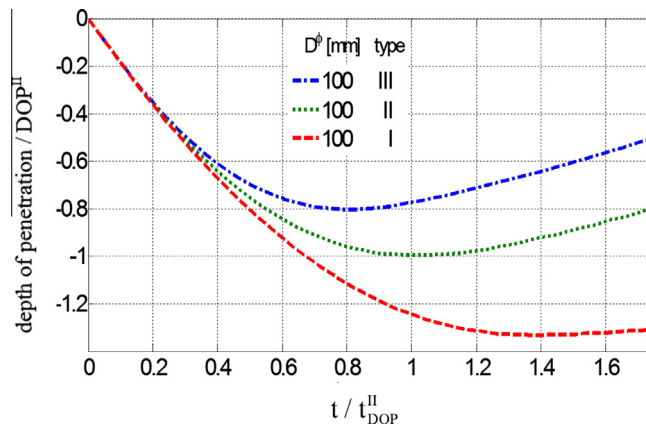


Fig. 17. The depths of penetration due to three cases of ductile failure strains.

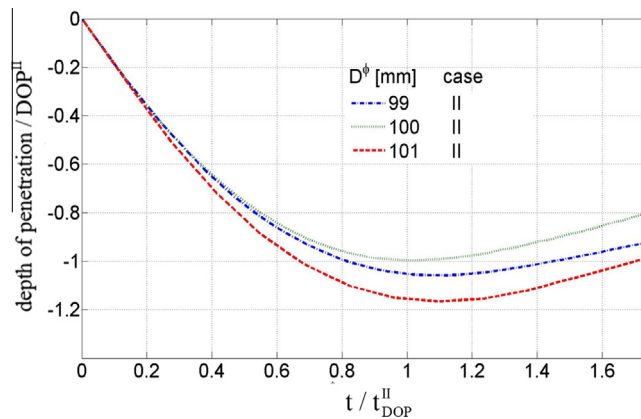


Fig. 18. The depths of penetrations due to three types of targets having different values of confinement prior to impact.

Table 3

Target details and their calculated maximum depth of penetration (DOP).

Target type	1	2	3
Larger cone diameter (mm)	100	101	99
Misfit (mm)	1.0	1.5	0.5
DOP (mm)	22.1	25.9	23.4
Normalized DOP	1.0	1.17	1.06

is 6% greater than the DOP of the 1st type target. This result shows that there is an optimal value of confinement which minimizes the ductile penetration. The penetration of the 1st type target is lower than the 3rd type because of its higher pressure which causes higher triaxiality that elevates the plastic failure strains according to Fig. 16(b). The penetration of the 2nd type target is greater than the 1st type even though it has higher pressure within it prior to impact (Fig. 5(a) and (b)). One may suggest that for a misfit greater than 1 (mm), the material is yielded and the slight increase in the pressure of the 2nd type does not cause a significant increase of its triaxiality (see Fig. 5(c) and (d)). The higher pressure within the 2nd type target was accompanied with higher Mises stress and plastic deformation, with no increase of triaxiality and

the failure strains. Hence the penetration of the 2nd type target was 17% deeper than that of the 1st type target. The optimum amount of confinement depends on the material properties such as yield stress and the plastic failure strains versus triaxiality.

## 5. Discussion

A hybrid experimental–numerical characterization of the behavior of thick confined and unconfined PMMA plates subjected to low velocity impact  $165 < V_0 < 260$  (m/s), of long steel ogive head projectiles have been conducted. The experimental results were complemented by numerical analyses which added insight regarding the effects of ductile failure strains and pre-impact confinement. The numerical results show good agreement with the experimental ones regarding the ductile damage, which essentially determines the trajectory of the projectile. As in part I, the numerical analyses fail to simulate the details of the brittle damage, namely crack propagation which originate in the ductile region around the trajectory.

In all of the reported experiments with the unconfined plates, complete perforation of the plates was achieved. The perforation was due to the combined ductile and



brittle damage. The projectiles penetrated the plates (ductile), and at the same time, radially propagating cracks (brittle) cause its rupture.

In all of the reported experiments with the confined plates, complete perforation of the plates was never achieved. One of the targets (target 4 Table 2) could even resist four impacts sequentially without complete perforation. The targets were partially penetrated and the limited brittle damage consisted essentially of hemispherical and dish-like, instead of radial, shallow cracks.

It was shown in part I that the two main failure mechanisms (ductile and brittle) operate simultaneously. The confinement seems to suppress both failure mechanisms. The brittle mechanism is suppressed due to the insertion pressure and negative triaxiality resulting from the confinement. The high pressure causes plastic deformation within the PMMA plate before impact (Fig. 5(e) and (f)) which increases the fracture toughness of the plate. These plastic deformations prior to impact (which correspond to high level of Mises stress) should have increased the ductile damage and resulted in deeper penetration. But deeper penetration does not occur because the ductile failure strains are triaxiality dependent. The plastic failure strains increase with negative triaxiality as was observed for metals (Dorogoy et al., 2011; Karp et al., 2013), hence the ductile penetration mechanism is suppressed as well.

The results of the numerical simulations also indicate that there is an optimal level of pressure which will result in a minimum ductile penetration. This level is related to the yield stress and the dependency of the plastic failure strains on the triaxiality.

Having understood the beneficial influence of the confinement on the ballistic performance of this polymer, one may nevertheless wonder about the long term duration of this improvement in relation to viscous relaxation phenomena which are characteristic of this class of materials. In particular, one might suspect that stress relaxation might affect the ballistic performance of the confined targets. The results reported by Archer and Lesser (2009) emphasized the important role of the hydrostatic stress, which when compressive, caused an increase in relaxation times. Moreover, Quale and Ravi-Chandar (2004) reported that the change in the bulk modulus is only a small fraction of that experienced by the shear modulus, and this result is in agreement with the generally accepted behavior for this polymer. Therefore, it seems that the pressure drop will be slower than that of the Mises stress, so that the *triaxiality will increase with time*, which can only improve the suppression of the ductile failure mechanism due to the elevation of failure strains. In other words, the confined targets will not only perform better under impact with respect to bare ones, but will also retain these improvements for long times.

## 6. Conclusions

- A new type of confinement was applied to PMMA plates by means of insertion into conical steel rings. This method provides control over the level of confinement

in an easy and straightforward manner that could potentially be applied to other classes of quasi-brittle materials such as ceramics.

- The observations of this work show beyond any doubt that confinement markedly increases the ballistic resistance of PMMA by significantly reducing both the ductile and brittle damage mechanisms.
- The higher the confinement the better the ballistic performance as long as the PMMA does not yield. There must be an optimum level of confinement which depends on the material properties.
- Due to the high confinement pressures and the slow time variation of the bulk modulus, it is expected that the viscoelastic nature of this glassy polymer will cause a very slow decrease in the ballistic performance with time. It can be shown that the level of triaxiality increases over time, which contributes to a long term reliability of the confined polymeric plate.

## Acknowledgments

The support of PMRI Grant # 2015267 is gratefully acknowledged. The assistance of Dr. A. Belenky, Mr. Y. Rotbaum, Mr. A. Godinger and Mr. Z. Shachar's with the high speed camera, photography and production of the sabots is greatly appreciated.

## References

- Abaqus/CAE Version 6.12-2, 2012. Dassault Systemes Simulia Corporation, Providence, RI, USA.
- Anderson, C.E., Royal-Timmons, S.A., 1997. Ballistic performance of confined 99.5%-Al<sub>2</sub>O<sub>3</sub> ceramic tiles. *Int. J. Impact Eng.* 19, 703–713.
- Arakawa, K., Mada, T., Takahashi, K., 2000. Correlations among dynamic stress intensity factor crack velocity and acceleration in brittle fracture. *Int. J. Fract.* 105, 311–320.
- Archer, J.S., Lesser, A.J., 2009. Impact resistant polymeric glasses using compressive pre-stress. *J. Appl. Polym. Sci.* 114, 3704–3715.
- Dorogoy, A., Karp, B., Rittel, D., 2011. A shear compression disk specimen with controlled stress triaxiality under quasi-static loading. *Exp. Mech.* 51, 1545–1557.
- Gasparini, D., 2006. The prestressing of structures: a historical review. In: *Proceeding of the Second International Congress on Construction History*, Queen's College, Cambridge University, vol. 2, pp. 1220–1232.
- Holmquist, T.J., Johnson, G.R., 2005. Modeling prestressed ceramic and its effect on ballistic performance. *Int. J. Impact Eng.* 31, 113–127.
- Holmquist, T.J., Johnson, G.R., 2003. Modeling projectile impact onto prestressed ceramic targets. *J. Phys. IV* 110, 597–602.
- Karp, B., Dorogoy, A., Rittel, D., 2013. A shear compression disk specimen with controlled stress triaxiality under dynamic loading. *Exp. Mech.* 53, 243–253.
- Loya, J.A., Villa, E.I., Fernández-Sáez, J., 2010. Crack-front propagation during three-point-bending tests of polymethyl-methacrylate beams. *Polym. Test* 29, 113–118.
- Nordin, H., 2005. Strengthening structures with externally prestressed tendons. Literature review, Luleå University of Technology Technical Report, 06.
- Quale, D., Ravi-chandar, K., 2004. Viscoelastic characterization of polymers under multiaxial compression. *Mech. Time-Depend. Mater.* 8, 193–214.
- Rittel, D., Dorogoy, A., 2013. Impact of thick PMMA plates by long projectiles at low velocities. Part I: Effect of head's shape. *Mech. Mater.* (in press). <http://dx.doi.org/10.1016/j.mechmat.2013.11.010>.
- Rittel, D., Maigre, H., 1996. An investigation of dynamic crack initiation in PMMA. *Mech. Mater.* 23, 229–239.